

Influence of the Applied Magnetic Field Strength on Flow Collimation in Magnetic Nozzles

Justin M. Little* and Edgar Y. Choueiri†

Electric Propulsion and Plasma Dynamics Laboratory, Princeton University, Princeton, NJ, 08544

The influence of the magnetic field strength on the collimation of the plasma flow in an electron-driven magnetic nozzle is investigated experimentally. A collimated plasma flow is required for efficient plasma propulsion to minimize plume divergence losses. Faraday probe measurements are used to estimate the ion streamlines in the diverging field of the magnetic nozzle. It is found that decreasing the strength of the applied magnetic field invokes a transition from a collimated plume to an under-collimated plume, where an under-collimated plume is defined such that the plume divergence is greater than the magnetic field divergence. Langmuir and emissive probe measurements reveal that the transition to an under-collimated plume is accompanied by anomalous deceleration of the ion beam along the nozzle centerline, broadening of the transverse density profile, and the disappearance of an ion-confining potential well at the plasma periphery. This transition offers a guideline for reducing the plume divergence of an electron-driven magnetic nozzle.

I. Introduction

Magnetic nozzles (MNs) are the primary acceleration stage of electrodeless electric propulsion systems such as the helicon plasma thruster (HPT),¹ electron cyclotron resonance thruster (ECRT),² and Variable Specific Impulse Magnetoplasma Rocket (VASIMR).³ In addition, MN-like effects are thought to be present in applied-field magnetoplasma dynamic thrusters (AF-MPDTs),⁴ and cylindrical and cusped-field Hall thrusters.⁵ While the diverging magnetic field of a MN is ubiquitous to these system, the fundamental effect of the MN on the plasma dynamics of each device varies depending on the presence of applied currents and disparate plasma species temperatures.

In this paper, we will concern ourselves primarily with MNs as used with HPTs and ECRTs, with the distinguishing quality being that the plasma source of these devices inherently heats electrons to much higher temperatures than ions ($T_e \gg T_i$). As a result, thermal expansion in the MN is driven by the hot electron population.⁶ We refer to magnetic nozzles that rely on this process as electron-driven magnetic nozzles (ED-MNs). Ion acceleration in an ED-MN results from the ambipolar electric field left in the wake of the hot electrons outrunning the colder ions.⁷ The diamagnetic current that results from magnetic confinement of the hot-electron plasma transfers momentum back to the magnetic circuit of the nozzle:⁸ an effect known as early as Seikel⁹ and recently demonstrated experimentally by Takahashi *et al.*¹⁰

Detailed experimental investigations of the fundamental processes of MNs have been limited to date, with recent efforts focused on the propulsion performance of thrusters that use MNs.^{11–15} Takahashi *et al.* showed¹² that the measured thrust approached the theoretical value predicted from a simplified analytical model¹⁶ as the applied field strength of an ED-MN increased. They attribute this behavior to decreased cross-field diffusion in the downstream plasma for increased applied magnetic fields, however, they do not study the source of this diffusion in depth.

Concern over the issue of plasma detachment from MNs has led to detailed investigations of the ion dynamics in the diverging field. Cox *et al.*¹⁷ and Deline *et al.*¹⁸ observed that the half-width at half-maximum of the radial density profile diverges less than the magnetic field, from which they conclude that ions have begun to detach from the MN. A similar conclusion was reached by Terasaka *et al.*¹⁹ using Mach probes to spatially map the three-dimensional ion velocity vector. Direct measurements of ion detachment

*Graduate Student, Research Assistant

†Chief Scientist, EPPDyL, Professor, Applied Physics Group, AIAA Fellow

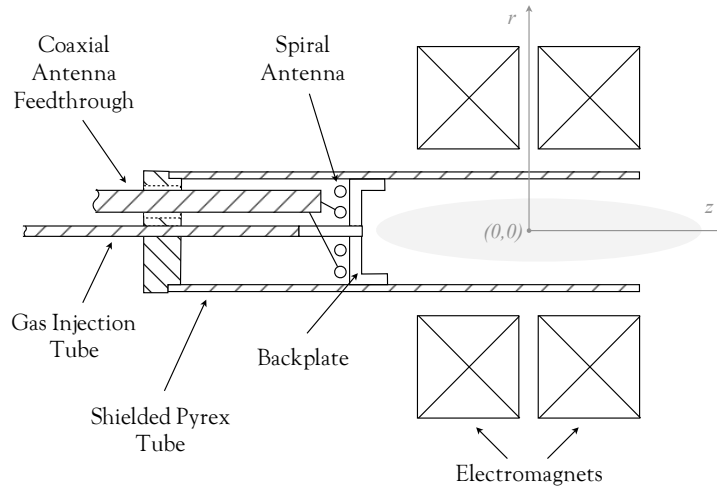


Figure 1. Diagram of the plasma source and magnetic nozzle.

were made using Faraday probe sweeps by Olsen *et al.*²⁰ In contrast to the previous studies, Olsen *et al.* observe that the ion streamlines of an ED-MN detach *outward* with respect to the diverging magnetic field. Using a second stage to energize the ion population in addition to the electron population, they find that the ion beam detaches *inward*: a phenomenon they attribute to anomalous electron cross-field transport driven by the increased ion momentum.

Many of these experiments have been performed at fixed or limited operational parameters. Notably absent from the literature is an experimental campaign addressing the influence of the applied magnetic field strength on both the ion dynamics of the magnetic nozzle and the density and potential structures in the flowing plasma. Therefore, the central goal of this study is to answer the question: How does the magnetic field strength influence the ion beam collimation in a MN exhaust? In the course of answering this question, we will remain focused on the relationship between the density and potential profiles and the ion beam divergence.

Our experimental setup, diagnostics, and parameter space are described in Sec. II. Measurements of the ion streamlines, ion beam energy, and transverse density and plasma potential profiles are presented in Sec. III. Finally, in Sec. IV we discuss the implications of the observed plasma dynamics on the performance of MNs for plasma propulsion.

II. Experimental Setup

In this section we provide a brief description of the plasma source and magnetic nozzle. We limit this description to the aspects of the experiment relevant to the present study, and encourage the reader to see Ref. [21] for a more detailed explanation of the system.

II.A. Plasma Source, Vacuum Chamber, and Magnetic Nozzle

The plasma source (Fig. 1) consists of a 7.5 cm inner diameter, 30.5-cm-long tube of borosilicate glass mounted concentrically inside two electromagnetic coils. A grounded copper mesh is wrapped around the outside of the glass tube to minimize stray electromagnetic radiation.

Argon gas is injected through the center of a Macor backplate. The backplate is adjustable within a range of approximately 10 cm to change the effective length of the plasma source. All of the data presented in this paper was taken at an Argon mass flow rate of $0.5 \text{ mg} \cdot \text{s}^{-1}$ with the backplate at a fixed location 18.5 cm upstream from the MN throat.

A two-turn spiral antenna positioned next to the backplate is used to excite the plasma using 13.56 MHz RF radiation. The antenna is connected to an L-type matching network via two rails that allow the antenna location to change along with the backplate. The power supply allows for approximately 750 W of delivered

power, however, the power is fixed at 500 W for the present study.

The plasma source is mounted in the EPPDyLs large dielectric pulsed propulsion (LDPP) vacuum chamber. The cylindrical chamber is made out of fiberglass and measures 8 ft in diameter and 25 ft in length. Two roughing pumps, a roots blower, and a 48 inch diameter CVC diffusion pump are used to achieve a base pressure around 40 μTorr . We then use liquid nitrogen baffles to further reduce the background pressure, with measured values as low as 8 μTorr . The steady-state pressure with the plasma source operating at 0.5 $\text{mg} \cdot \text{s}^{-1}$ Ar was measured to be around 20 μTorr .

A MN is formed by passing DC current through the electromagnets. The strength of the magnetic field, B , is controlled with the applied current, I_B , such that $B[\text{G}] \approx 21I_B[\text{A}]$. The magnets are capable of operating at 50 A of current, however, we limited our measurements to applied currents less than 20 A due to the presence of an antenna-plasma coupling mode transition near this value. Although it has not been confirmed using magnetic probe measurements, Langmuir probe measurements of the density and electron temperature suggest that we are operating in a low-field helicon mode prior to this transition.²²

The effective radius of each coil is located at $r_c = 7.51$ cm, which roughly corresponds to the physical radius of the center of the coil windings. Although they were designed to move freely with respect to each other and the plasma source, in this study the magnets are rigidly connected with an axial separation of 4.5 cm between their effective centers. The downstream face of the magnet pair is mounted such that it is flush with the opening of the glass tube.

II.B. Plasma Diagnostics

Four different diagnostics are used throughout this study: an RF-compensated Langmuir probe, an emissive probe, a Faraday probe, and a retarding potential analyzer. A rotating translation stage allows accurate positioning of the probes over a large domain within the r - z plane. The locations at which we take measurements with each probe are depicted in Fig. 2. Here, “ \times ”s and “ $+$ ”s denote single-point measurements taken in the plume and radially along the MN throat plane, respectively, while solid lines indicate a measurement sweep along the line with a sampling rate determined by the specific probe.

The RF-compensated Langmuir probe (RF-LP) is based on the design by Sudit and Chen²³ that uses chip inductors and an auxiliary electrode to increase the probe impedance at the RF frequency and its first harmonic. Current-voltage (IV) traces are obtained for single-point measurements, which yield the plasma density and electron temperature. The ion saturation current is collected during the measurement sweeps to determine the plasma density profile along each arc.

We find that the conventional methods for determining the plasma potential from the Langmuir probe IV curve exhibit significant errors; therefore, we measure the plasma potential using an emissive probe (EP).²⁴ The emissive probe is made by friction fitting a tungsten filament between two copper wires separated from each other by the wall of a two-bore alumina tube.²⁵ We heat the filament to electron emission using half-wave rectified AC current and measure the floating potential of the probe. Using the floating point method, the plasma potential is obtained from the rectified portion of the floating potential signal.²⁶

Ion current densities in the exhaust plume are obtained using measurement sweeps of a Faraday probe (FP).²⁷ The current collecting surface of the probe is mounted flush within a guard-ring, which is used to minimize the error due to sheath effects on the collection area. Current is collected through a shunt resistor for probe and guard-ring bias voltages of -30 V.

Finally, a four-grid retarding potential analyzer (RPA)²⁸ is used to measure the ion beam energy along the centerline of the plume. The IV trace of the RPA is obtained by applying a voltage sweep between 0 V and 80 V to the ion repelling grid and measuring the current to the grounded ion collection disc. A DC bias of -15 V is applied to each of two electron repelling grids to minimize the effect of secondary electrons. The ion energy distribution function is obtained from the derivative of the IV-curve, which can be combined with the plasma potential measurement to indicate the presence and energy of the ion beam.

III. Magnetic Nozzle Plasma Dynamics

While theoretical and computational models have taught us much about the plasma dynamics of a magnetic nozzle, there is a limited database of experimental data to validate these models, test their predictions, and drive new insight. To fill this knowledge gap, we focus in this section on the prediction that the plasma dynamics of a MN are independent of the applied magnetic field strength, except for at very low²⁹ or very

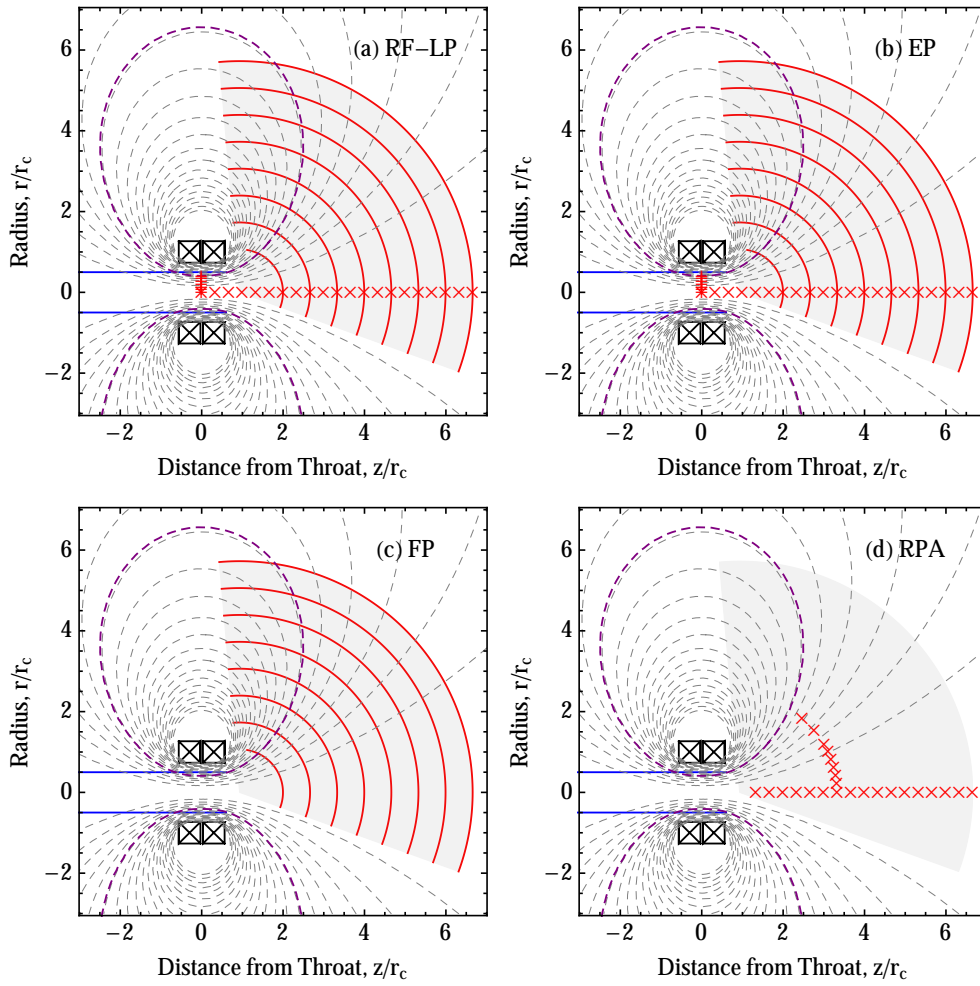


Figure 2. Measurement locations for the (a) RF-compensated Langmuir probe, (b) emissive probe, (c) Faraday probe, and (d) retarding potential analyzer. “x”s and “+”s denote single-point measurements along the centerline and throat plane, respectively. Measurement sweeps are shown as red lines while the gray dashed lines show the magnetic flux surfaces. The purple dashed line is the magnetic flux surface that intersects the glass chamber of the plasma source, which is shown as a solid blue line.

high magnetic fields.⁸ Specifically, we will use experimental data to answer the question posed at the outset: how does the magnetic field strength influence the ion beam collimation in a MN exhaust?

III.A. Ion Dynamics

The performance of a MN depends strongly on the divergence of the exhaust beam, with a collimated beam required to minimize divergence losses. The beam divergence is intimately related to the ion dynamics in the plume because the ions carry most of the momentum by virtue of their large mass compared to the electron mass. Here, we characterize the influence of the applied magnetic field strength on the ion dynamics by measuring the ion streamlines and beam energy at different plume locations.

Following the method of Olsen *et al.*,²⁰ we can estimate the location of the ion streamlines by measuring the ion current density profile using the swept Faraday probe (see Fig. 2(c)). The streamlines may be found by solving for the location, $\theta_{ts} = \theta_\chi$, at which the area integral of the current density is a certain fraction, χ , of the total current, or

$$\chi = \int_0^{\theta_\chi} j_i \sin \theta_{ts} d\theta_{ts} \Big/ \int_0^{\theta_{\max}} j_i \sin \theta_{ts} d\theta_{ts}. \quad (1)$$

Here, j_i is the ion current density measured using the Faraday probe, θ_{ts} is the angle that the translation stage makes with the MN centerline and $\theta_{\max} = 95^\circ$ is the maximum angle allowed by the translation stage

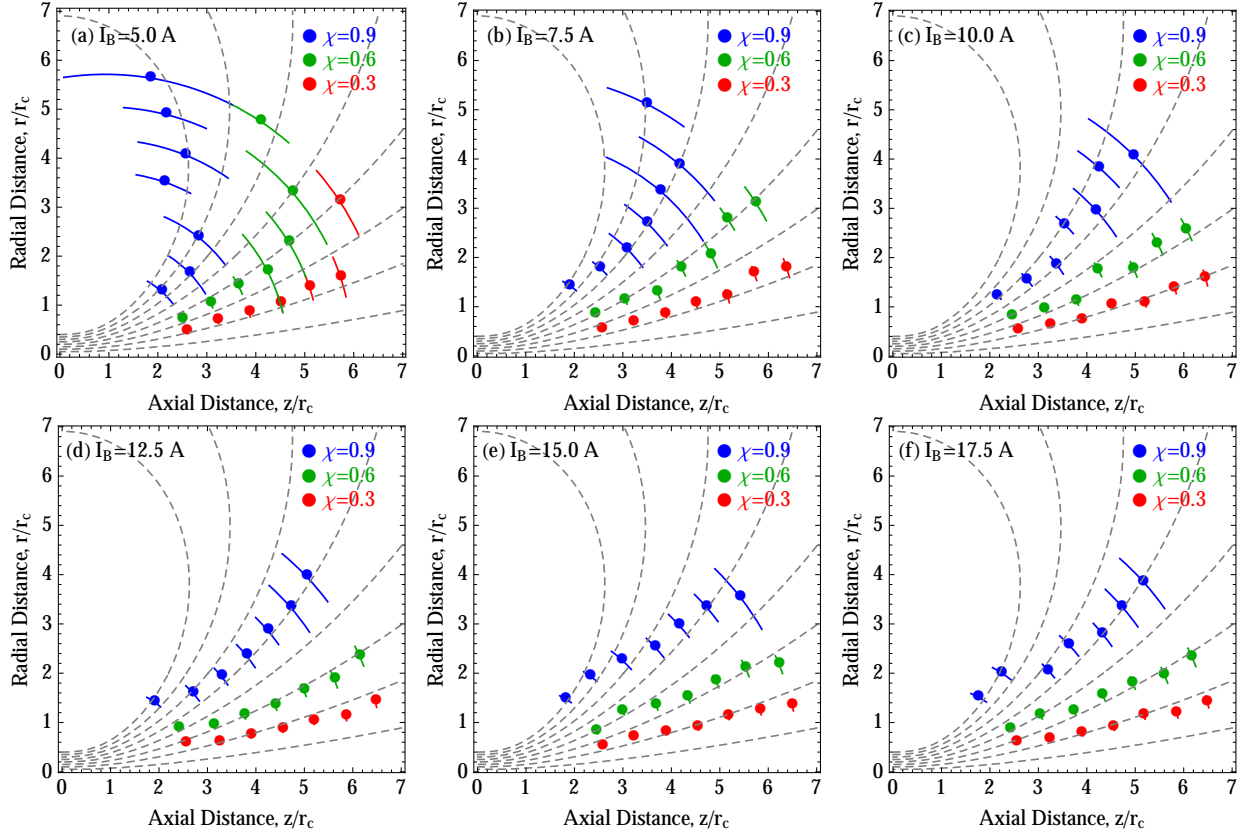


Figure 3. Location of the ion streamlines containing (red) 30%, (green) 60%, and (blue) 90% of the total ion current for various (a)-(f) applied field strengths. Dashed lines depict the magnetic flux surfaces, which are bounded by the magnetic flux surface that intersects the glass chamber of the plasma source.

for our system.

The locations of the ion streamlines for different magnet currents are shown in Figs. 3(a)-(f) along with the magnetic flux surfaces (dashed lines) of the nozzle. Each figure contains three different data sets that represent the streamlines containing 30%, 60%, and 90% of the total ion current. Note that the error bar is indicative of the signal-to-noise ratio for each measurement. The signal-to-noise ratio scales with the density of the plasma, which is generally lower towards the plasma periphery and for small I_B (due to decreased confinement in the plasma source).²¹

We immediately notice that the ion streamlines become more collimated as the applied magnetic field strength increases. Qualitatively, the streamlines for $I_B = 5.0$ diverge faster than the magnetic field lines, while the streamline and field line divergence for $I_B = 7.5$ A is comparable. As I_B increases beyond 10 A the streamlines become less divergent than the field lines. For $I_B \geq 15.0$, this is accompanied by significant cross-field motion of the ions and linearization of the streamline in the far-field. We note that linear streamlines in the far-field were observed by Olsen *et al.*,²⁰ and have been used as a criteria for ion detachment from the MN.

Clearly a transition in the dynamics of the flow through the MN is occurring near $I_B = 5.0$ A. We define this transition in terms of the collimation of the plume, which we will quantify momentarily. Specifically, we will refer to flow that diverges *more* than the applied magnetic field as *under-collimated*. Alternatively, flow that diverges *less* than the magnetic field will be regarded as *collimated*.

The plume divergence may be quantified using the divergence half-angle of the ion beam, θ_{div} , such that

$$\cos \theta_{\text{div}} = \int_0^{\theta_{\text{max}}} j_i \cos \theta_{\text{ts}} \sin \theta_{\text{ts}} d\theta_{\text{ts}} / \int_0^{\theta_{\text{max}}} j_i \sin \theta_{\text{ts}} d\theta_{\text{ts}}. \quad (2)$$

Quantifying the magnetic field divergence is more obscure, however, because different magnetic field lines diverge at different rates. Furthermore, the ion current density is largest towards $r = 0$, which means that

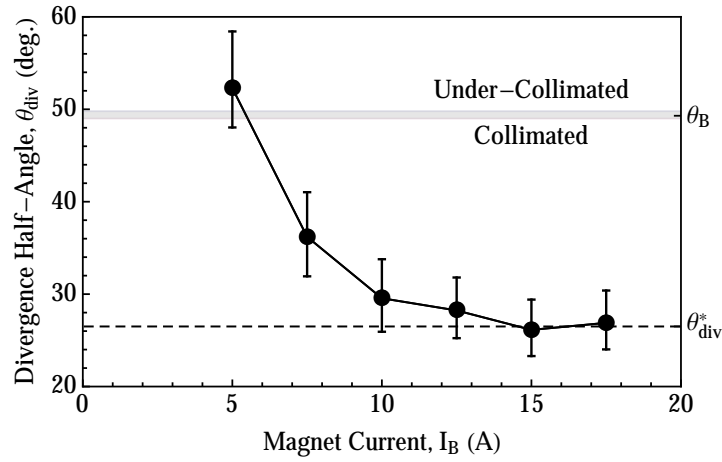


Figure 4. Exhaust plume divergence half-angle, θ_{div} , versus magnet current, I_B , demonstrating the transition from an under-collimated flow to a collimated flow. The grey region represents the range of values corresponding to the magnetic field divergence, θ_B , for different I_B . The dashed line is the approximate asymptotic value of the divergence half-angle, θ_{div}^* .

the plume divergence is weighted towards the MN centerline. To account for this, we calculate the magnetic field divergence, θ_B , as the *hypothetical* plume divergence if the ion current density profile remained constant (i.e. self-similar) throughout the plume, which would be true if the ion streamlines followed the magnetic field lines. We use RF-LP measurements to estimate the ion current density profile at the MN throat, j_0 . We then substitute $j_i \rightarrow j_0 \cos(\Delta\theta_p)$ and $\theta_{div} \rightarrow \theta_B$ into Eq. (2) to solve for θ_B , where we have defined $\Delta\theta_p$ as the angle that the magnetic field vector makes with the probe.

The results of this quantification may be seen in Fig. 4 where we plot the divergence half-angle as a function of the magnet current. Here, we use the furthest downstream FP sweep to determine θ_{div} . The shaded region represents the range of θ_B -values calculated using the RF-LP measurements at the MN throat for the different I_B . In accordance with our qualitative analysis of Fig. 3, we observe a transition from an under-collimated flow to a collimated flow near $I_B = 5.0$ A. As I_B increases the flow becomes collimated as the beam diverges less than the magnetic field. Eventually, we observe the divergence half-angle to approach an asymptote, $\theta_{div}^* \ll \theta_B$.

We note that it is predicted that the plume divergence should increase at high magnetic fields due to the effect of the Lorentz force on the ion trajectories. The magnetic field strength at which the Lorentz force has an appreciable effect on the ion motion can be approximated by $B_0^* [\text{kG}] \approx 0.1\sqrt{\mu_i T_{ev}}$,⁸ where μ_i is the ion atomic number. For our plasma ($\mu_i = 40$, $T_{ev} \approx 7$ eV), the required magnetic field is $B_0^* \approx 1.7$ kG. The maximum operating magnetic field of our magnets is $B_{max} \approx 1.0$ kG. Furthermore, for the operating parameters focused on in this study, the helicon mode is only stable for $B_w \leq 0.45$ kG.²¹ We are therefore restricted in our experiments to operate under the threshold magnetic field at which ion magnetization becomes important.

We further characterize the ion dynamics by measuring the energy of the ion beam at different locations along the MN centerline using the RPA (see Fig. 2(d)). IV curves are obtained by sweeping the ion repeller grid voltage and measuring the current at the ion collector.²⁸ The ion energy distribution function (IEDF) follows from the derivative of this curve,

$$f_i(V) \propto \frac{1}{\sqrt{V}} \frac{dI}{dV}. \quad (3)$$

The IEDF is expressed in Eq. (3) in terms of the ion repeller voltage, V , which is related to the ion velocity, v_i , and the local plasma potential, V_p , through

$$e(V - V_p) = \frac{1}{2} m_i v_i^2. \quad (4)$$

Plots of the axial evolution of the IEDF in the MN plume for different magnet currents are shown in Figs. 5(a)-(f) as gray lines. The black data points correspond to the plasma potential measurements obtained with the EP. The separation between the IEDF peak and the plasma potential is a clear indication

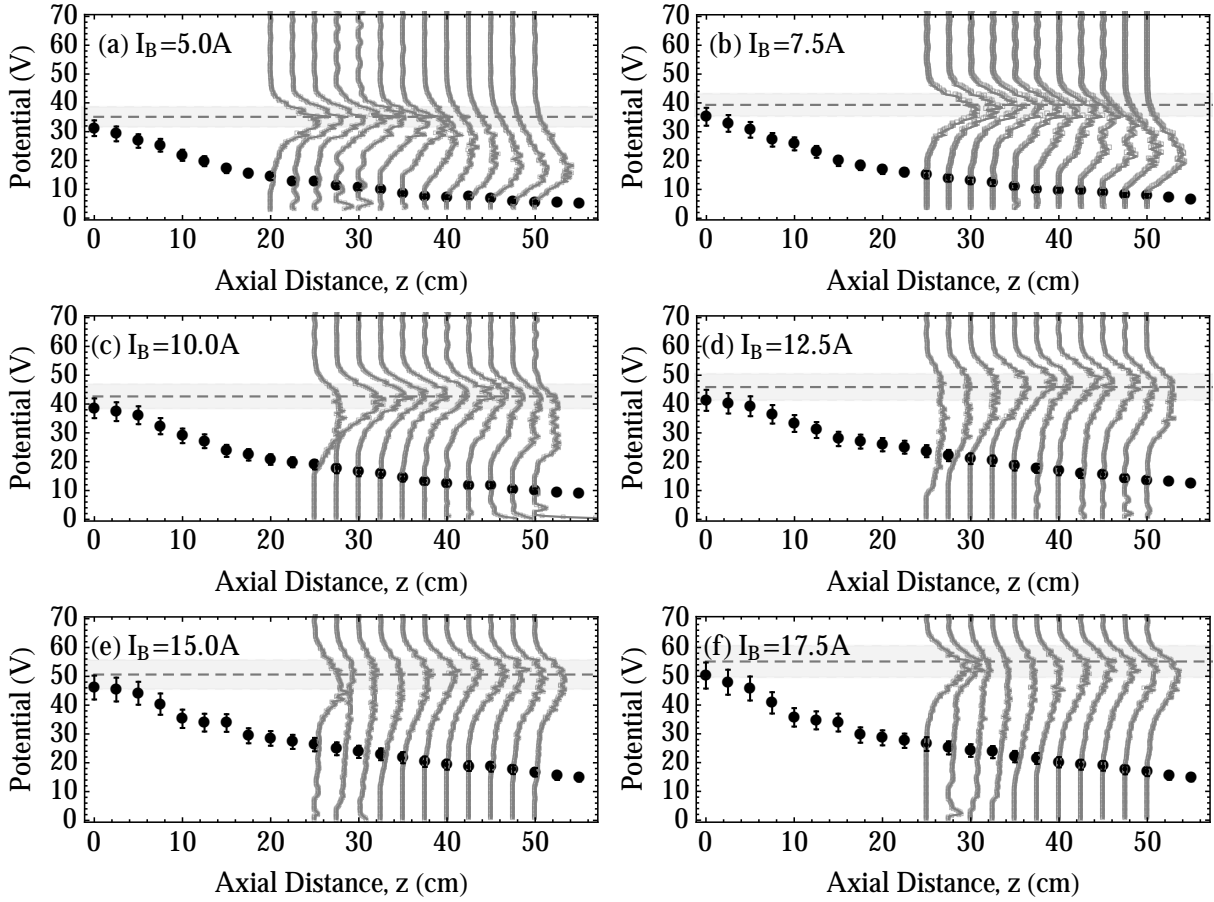


Figure 5. Plasma potential (black) and ion energy distribution function (grey) measurements for various magnetic field strengths (a)-(f). The units of the IEDF are arbitrary and normalized such that they possess a constant area. The dashed line corresponds to the expected beam voltage for a choked nozzle, with the shaded region representing the experimental uncertainty of this assumption.

that a supersonic ion beam has formed in the exhaust. Furthermore, in contrast to similar devices in the literature,^{14,15,30} a peak near the plasma potential is not typically found in our data, which indicates that the fraction of beam ions to background ions along the centerline remains large.

It is often assumed that the flow at the MN throat is choked,³¹ which implies that the average ion velocity at this location is equal to the ion acoustic speed, $c_s = \sqrt{\gamma_e T_e / m_i}$. Under this assumption, the initial ion beam voltage is related to the plasma potential at the throat, $V_{p,t}$, the electron polytropic index, γ_e , and the electron temperature at the throat, $T_{e,t}$ in the following manner

$$V_{b,t} = V_{p,t} + \frac{\gamma_e}{2} T_{e,t}, \quad (5)$$

where $T_{e,t}$ is expressed in terms of electron volts. Furthermore, it is possible to show that the beam voltage of the ions remains constant if the dominant force on the ions is the ambipolar electric field.

Therefore, it should be expected that the peak of the IEDF approximately coincides with $V_{b,t}$ in the downstream region, which is indeed the case. The voltage corresponding to $V_{b,t}$ is labelled by a dashed line in Fig. 5, with the shaded region representing the error due to measurements of $V_{p,t}$ and $T_{e,t}$. It is clear that over large regions of the plume the IEDF peak occurs near the same voltage. Furthermore, this peak voltage is approximately $V_{b,t}$, which implies that the sonic condition is met at the MN throat.

Interesting deviations from the expected behavior of a supersonic ion beam under the influence of ambipolar electric fields are observed as I_B decreases. For $I_B \leq 12.5$ A, there exists a specific location where the beam begins to decelerate. This location depends on I_B , and is pushed further upstream as I_B decreases.

Surprisingly, this deceleration is not due to steady state electric fields as is indicated by the fact that the plasma potential continues to decrease in this region.

It could be reasonably expected that the observed deceleration is due to collisions of the beam ions with background neutrals. Using conservative estimates for the total collisional cross section and background pressure near the exhaust, $\sigma_{Ar} \sim 7 \times 10^{-19}$ and $P_{bg} \sim 40 \mu\text{Torr}$, the expected mean free path for collisions between the ion beam and background gas is $\lambda_{mfp} \sim 1$ m. The beam begins to decelerate well before this location. Furthermore, a gradual deceleration would be expected if the beam were interacting with the background gas. Rather, the effective deceleration length scale is around $\lambda_d \sim 6$ cm. Therefore, it would seem that the transition from a collimated flow to an under-collimated flow is coincident with anomalous deceleration of the ion beam, whose location approximately coincides with the region of increased beam divergence.

III.B. Electron Cooling, the Polytrropic Law, and the Boltzmann Distribution

In the previous section we used the electron polytropic index, γ_e , to calculate the expected ion beam voltage assuming choked flow at the nozzle throat. We show here the method used to estimate γ_e and examine the influence of the applied magnetic field strength on its value.

Theoretical models that assume isothermal expansion of the electrons are inherently problematic due to the fact that an infinite flux of heat from the PS to MN is required to maintain a constant electron temperature. To remove this inconsistency, a polytropic law³² may be introduced that assumes that the electron temperature decreases according to

$$\mathbf{B} \cdot \nabla \left(\frac{p_e}{n^{\gamma_e}} \right) = 0. \quad (6)$$

Here, \mathbf{B} is the magnetic field vector and $p_e = nT_e$ is the electron pressure.

It has been shown using theoretical models that the value of the polytropic exponent strongly influences the resulting behavior and performance of the MN.^{33–35} Unfortunately, there is very little theoretical support for the polytropic law, and calculation of γ_e from existing experimental data provides little consensus with values ranging from $\gamma_e \leq 1$ to $\gamma_e > 5/3$.^{18,36,37}

RF-LP and EP measurements of the density, electron temperature, and plasma potential along the axis of the MN (see Fig. 2) allow us to accurately estimate γ_e for our experiment using two different methods. First, the definition of a polytropic process, Eq. (6), implies that

$$\left. \frac{d[\log_{10}(n)]}{d[\log_{10}(T_e)]} \right|_{\psi} = \gamma_e - 1. \quad (7)$$

Thus, measurements of T_e and n_e at different axial locations along the MN centerline (constant ψ) yield γ_e from the slope of the $\log_{10}(n)$ vs. $\log_{10}(T_e)$ curve. Furthermore, the electron momentum equation and Eq. (6) may be used to relate the plasma potential and electron temperature

$$\left. \frac{dV_p}{dT_e} \right|_{\psi} = \frac{\gamma_e}{\gamma_e - 1}. \quad (8)$$

Here, we have made use of the fact that the electron centrifugal and Lorentz forces go to zero as $r \rightarrow 0$. Furthermore, the small mass of electrons means that electron inertia is negligible.

We plot in Figs. 6(a)-(f) the data used to calculate γ_e using Eqs. (7) and (8) for two different values of I_B . The solid black lines correspond to the least-squares fit to the measured data, while the gray shaded region represents the 95% confidence interval. Also shown is the value of γ_e and its error calculated from the slope and slope error of the least-squares fit using Eqs. (7) and (8).

We conclude from Fig. 6 that the polytropic law for electron cooling accurately describes the relationship between the electron temperature and plasma density over a wide region of the plume. We cannot rule out the possibility, however, that localized areas of increased or decreased cooling exist due to the limited fidelity of the RF-LP measurements. Rather, the polytropic law can be viewed as a global estimate of the electron energy flux from the MN. A deeper theoretical understanding of the electron thermal conductivity in the exhaust plume is required to understand the apparent validity of the polytropic law and explain the measured value of γ_e .

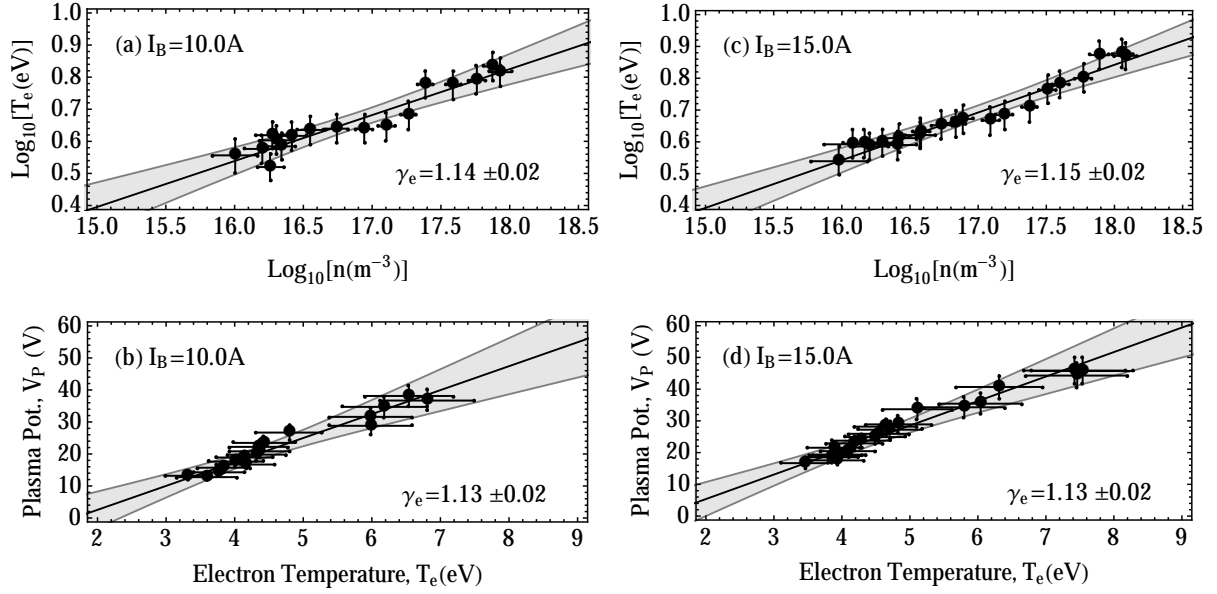


Figure 6. Plots demonstrating the linearity between the measured quantities $\log_{10}(n)$ and $\log_{10}(T_e)$ for (a) $I_B = 10 \text{ A}$, (c) $I_B = 15 \text{ A}$, and (e) $I_B = 20 \text{ A}$, and the measured quantities V_p and T_e for (b) $I_B = 10 \text{ A}$, (d) $I_B = 15 \text{ A}$, and (f) $I_B = 20 \text{ A}$. The solid black lines and shaded regions show the resulting least-squares fit to the data along with the 95% confidence interval.

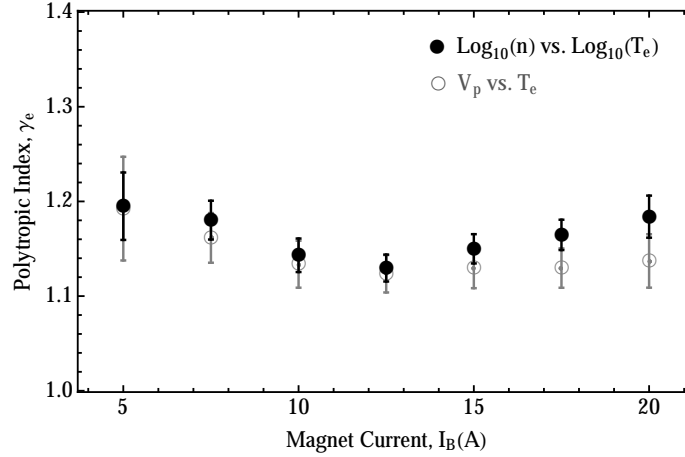


Figure 7. Magnetic field strength dependence of the electron polytropic index measured using the two methods indicated in the figure legend.

A comparison between the values of γ_e calculated using Eqs. (7) and (8) for different I_B is shown in Fig. 7. The two methods of calculating γ_e exhibit remarkable agreement, with the largest discrepancy between measurements of about 3%, which is well within the measurement errors. The observed changes in γ_e with I_B fall within the measurement errors of each technique, thus we cannot conclude if the applied field strength affects γ_e . However, we note that γ_e varies by only 6% for the data shown in Fig. 7. This variation is small compared to the range of values between isothermal ($\gamma_e = 1$) and isentropic ($\gamma_e = 5/3$) processes.

Finally, it has been reported³⁸ that electron expansion in a MN follows the Boltzmann distribution, or $n = n_0 \exp(-\Delta V_p/T_e)$. This distribution results from the electron momentum equation projected along the magnetic field in the limit of negligible electron inertia and isothermal electrons. It is clear from Fig. 6 that the isothermal assumption is not technically valid in the exhaust plume. However, Eq. (8) implies that changes in V_p are much greater than changes in T_e , meaning the Boltzmann distribution between n and V_p

will hold to within the experimental uncertainty of most diagnostics.

III.C. Exhaust Structure and Plasma Confinement

We observed in Sec. III.A a transition from an under-collimated to a collimated exhaust plume as the applied magnetic field strength increased above a certain value. Here, we use RF-LP and EP measurements to obtain the transverse density and plasma potential profiles at various locations in the exhaust to gain insight on the physical mechanism behind the collimation transition. Throughout our analysis we will refer to the probe location that corresponds to θ_{ts} as z_0 .

Density profiles are obtained from the ion saturation current, I_{sat} , of the RF-LP using a -27 V bias. An estimation for the electron temperature is required to determine the density from I_{sat} . For this, we use the polytropic law (Eq. (6)) to relate the local electron temperature to the local density at the measurement location using measurements of the electron temperature and density at the MN throat, the value of γ_e determined from the axial RF-LP data (see Sec. III.B), and the known magnetic field topology. Therefore, this technique allows us to estimate the density anywhere in the plume using only I_{sat} .

The normalized plasma density profile for a centerline probe location of $z_0 = 30$ cm can be seen for different applied magnetic field strengths in Fig. 8. Here, the density profile is normalized by the density at the MN centerline, n_{cl} . Also shown is a dashed line that represents the location of the predicted plasma-vacuum flux surface, θ_p , which coincides with the magnetic flux surface that intersects the glass tube at the plasma source exit.

The plasma density is clearly peaked towards the MN centerline in all cases. The density profile is most narrow at high magnetic fields and seems to approach an asymptotic value. The density profile broadens significantly as the magnetic field is decreased, which agrees with the observation that the divergence of the ion streamlines increases as the magnetic fields strength decreases. Because the density and temperature profiles at the MN throat were measured to be similar regardless of the magnet current, we conclude that the observed density profile broadening is due to increased cross-field diffusion of the downstream plasma. Classical diffusion cannot be invoked to explain the broadening due to the low plasma densities in this region, thus we suspect that some form of anomalous transport is present.

The influence of I_B on the plasma potential profile is shown in Figs. 9(a)-(f) for six different z_0 . The normalized plasma potential is given by $\phi = (V_p - V_{p,0})/T_0$, where $V_{p,0}$ and T_0 are the plasma potential and electron temperature at the MN throat, respectively. Furthermore, ϕ_{cl} is the value of ϕ along the MN centerline. Again, the dashed line in each figure coincides with the predicted plasma boundary.

Similar to the density profiles, it is observed that the plasma potential profile is peaked towards the MN centerline. This is due to the transverse electric field that forms to maintain quasineutrality at the plasma periphery.⁸ The most interesting feature, and one that is not predicted from existing theoretical models, is the potential structure that forms near the predicted plasma edge (see Fig.9(a)). Here, we observe the

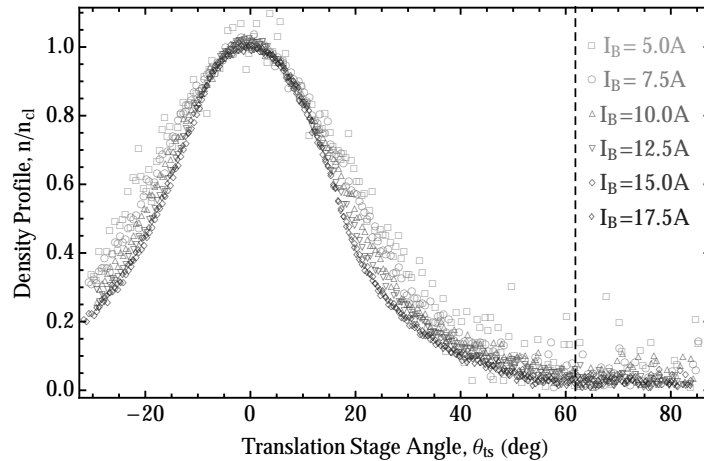


Figure 8. Normalized transverse plasma density profile for various magnet currents, I_B . The dashed line represents the predicted plasma-vacuum boundary, which coincides with the magnetic flux surface that intersects the glass tube at the plasma source exit.

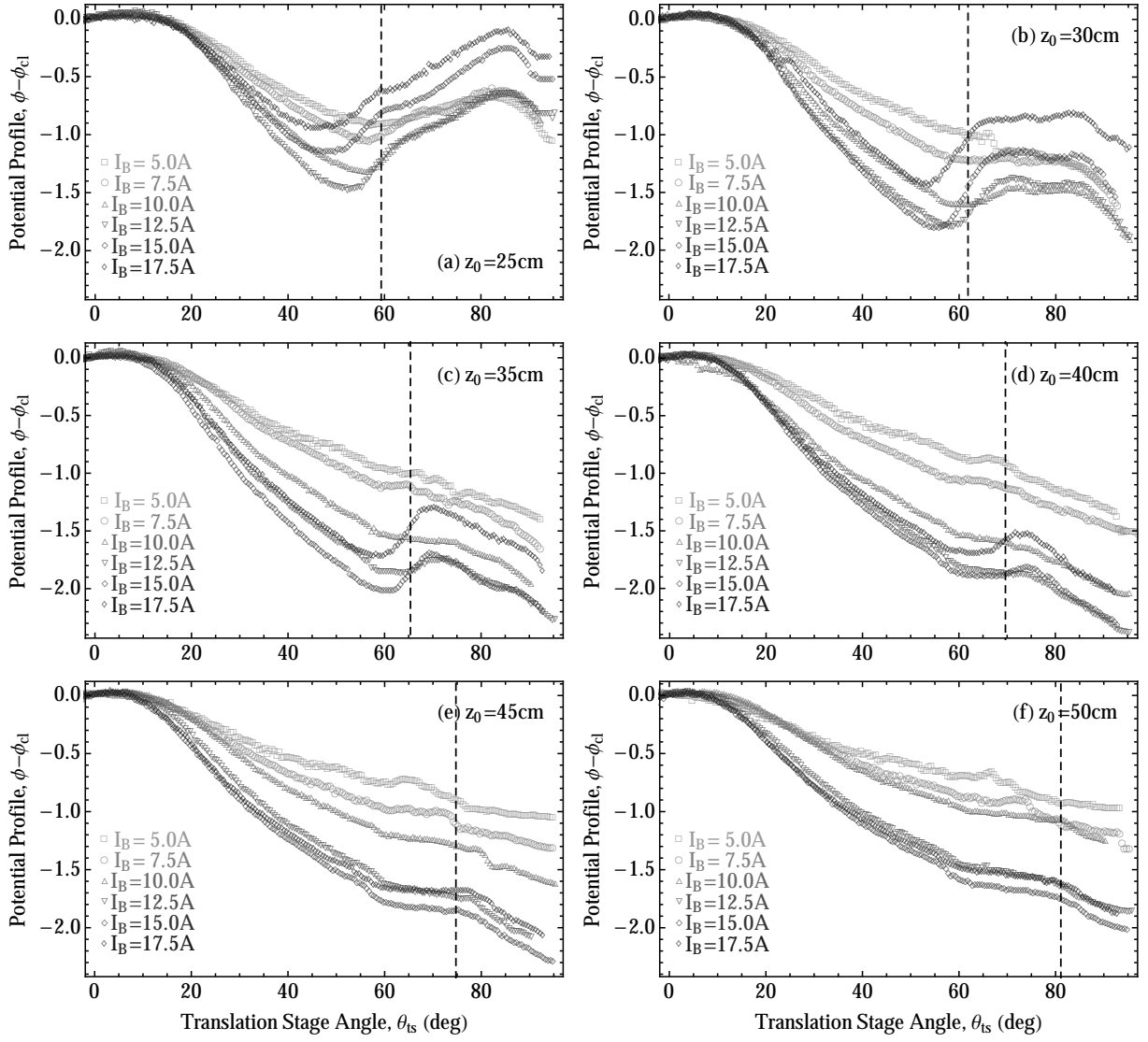


Figure 9. Normalized transverse plasma potential profiles for various magnet currents, I_B , and (a)-(f) centerline probe locations, z_0 . The dashed vertical line represents the predicted plasma-vacuum boundary, which coincides with the magnetic flux surface that intersects the glass tube at the plasma source exit.

formation of a potential well near θ_p . The potential well implies that the transverse electric field switches direction, from outward to inward, near the edge of the plasma. A similar potential structure was predicted using PIC simulations³⁹ and verified experimentally⁴⁰ using a helicon plasma expanding along magnetic field lines into a grounded diffusion chambers. In both of these studies the plasma density was observed to accumulate near the potential well, which is in contrast to our observations (see Fig. 8).

Keeping in mind that the magnitude of the normalized transverse electric field scales with the gradient, or slope, of the potential profile, we observe the following from Figs. 9(a)-(f): (1) The magnitude of the inward electric field generally increases with increasing I_B ; (2) The location of the maximum inward electric field moves closer to the MN centerline as I_B increases; (3) The potential well ultimately disappears at a downstream location that increases with I_B ; and (4) the disappearance of the potential well for the under-collimated plume approximately coincides with the location at which the ion streamlines being to diverge faster than the magnetic field lines, according to Fig. 3(a).

IV. Conclusion

Using detailed measurements of the ion dynamics and plasma density and potential structure within an expanding magnetic nozzle plasma we are able to conclude the following:

- There exists a transition from an under-collimated plume mode to a collimated plume mode with increasing applied magnetic field strengths, where an under-collimated plume is defined such that the plasma expands at a greater rate than the applied magnetic field.
- The energy of the ion beam corresponds well with the value predicted by ambipolar acceleration through the electric field generated in the wake of an expanding population of hot electrons. Deceleration of the ion beam correlates with the outwards diffusion of the plasma at low magnetic fields, and cannot be explained by electrostatic forces or background effects.
- Electron cooling in the expanding plasma approximately follows a polytropic law, with γ_e independent of the applied magnetic field strength to within experimental uncertainties.
- The transverse plasma density profile is peaked towards the MN centerline and asymptotically approaches a similar shape for high magnetic fields. Significant broadening of the density profile occurs at low applied magnetic fields, which implies increased cross-field diffusion.
- Increased plume expansion is correlated with the disappearance of an ion-confining potential well near the location of the bounding magnetic flux surface. The magnitude of the inward-directed normalized electric field that results from this potential well increases with the applied magnetic field strength.

The above findings are in agreement with the increased MN performance at large applied magnetic fields recently observed by Takahashi *et al.*¹³ The physical mechanism that leads to this loss of confinement remains to be seen, however. One possibility is that the plasma detaches outwards with respect to the magnetic field for under-collimated plumes because the residual thermal energy of the electrons can no longer be magnetically confined.²⁹ In a sense, the magnetic nozzle is under expanded. We will test this prediction, along with other theoretical detachment models, in a future study.

Acknowledgments

The authors gratefully acknowledge Mark A. Hopkins and Prof. Lyon B. King of the ISP lab at Michigan Tech for allowing us to borrow their retarding potential analyzer.

References

- ¹Winglee, R., Ziemba, T., Giersch, L., Prager, J., Carscadden, J., and Roberson, B., "Simulation and laboratory validation of magnetic nozzle effects for the high power helicon thruster," *Phys. Plasmas*, Vol. 14, 2007, pp. 063501.
- ²Bethke, G. W. and Miller, D. B., "Cyclotron resonance thruster design techniques," *AIAA J.*, Vol. 4, No. 5, 1966, pp. 835–840.
- ³Longmier, B. W., Cassady, L. D., Ballenger, M. G., Carter, M. D., Chang-Díaz, F. R., Glover, T. W., Ilin, A. V., McCaskill, G. E., Olsen, C. S., Squire, J. P., and *et al.*, "VX-200 magnetoplasma thruster performance results exceeding fifty-percent thruster efficiency," *J. Propul. Power*, Vol. 27, No. 4, 2011, pp. 915–920.
- ⁴Sasoh, A. and Arakawa, Y., "Thrust formula for applied-field magnetoplasma dynamic thrusters derived from energy conservation equation," *J. Propul. Power*, Vol. 11, No. 2, 1995, pp. 351–356.
- ⁵Fruchtman, A., Gueroult, R., and Fisch, N., "Rigid-body rotation of an electron cloud in divergent magnetic fields," *Phys. Plasmas*, Vol. 20, No. 7, 2013, pp. 073502.
- ⁶Kuriki, K. and Okada, O., "Experimental study of a plasma flow in a magnetic nozzle," *Phys. Fluids*, Vol. 13, 1970, pp. 2262.
- ⁷Cohen, S. A., Siefert, N. S., Stange, S., Boivin, R. F., Scime, E. E., and Levinton, F. M., "Ion acceleration in plasmas emerging from a helicon-heated magnetic-mirror device," *Phys. Plasmas*, Vol. 10, 2003, pp. 2593.
- ⁸Ahedo, E. and Merino, M., "Two-dimensional supersonic plasma acceleration in a magnetic nozzle," *Phys. Plasmas*, Vol. 17, 2010, pp. 073501.
- ⁹Seikel, G. R., "Generation of thrust-electromagnetic Thrusters," *Electric Propulsion for Spacecraft*, Vol. 22, 1962, p. 19.
- ¹⁰Takahashi, K., Lafleur, T., Charles, C., Alexander, P., and Boswell, R. W., "Electron Diamagnetic Effect on Axial Force in an Expanding Plasma: Experiments and Theory," *Phys. Rev. Lett.*, Vol. 107, No. 23, 2011, pp. 235001.
- ¹¹Takahashi, K., Lafleur, T., Charles, C., Alexander, P., Boswell, R., Perren, M., Laine, R., Pottinger, S., Lappas, V., Harle, T., et al., "Direct thrust measurement of a permanent magnet helicon double layer thruster," *Appl. Phys. Lett.*, Vol. 98, No. 14, 2011, pp. 141503–141503.

- ¹²Takahashi, K., Charles, C., Boswell, R. W., and Ando, A., "Performance improvement of a permanent magnet helicon plasma thruster," J. Phys. D: Appl. Physics, Vol. 46, No. 35, 2013, pp. 352001.
- ¹³Takahashi, K., Charles, C., and Boswell, R. W., "Approaching the Theoretical Limit of Diamagnetic-Induced Momentum in a Rapidly Diverging Magnetic Nozzle," Phys. Rev. Lett., Vol. 110, No. 19, 2013, pp. 195003.
- ¹⁴Williams, L. T. and Walker, M. L. R., "Thrust measurements of a radio frequency plasma source," J. Propul. Power, Vol. 29, No. 3, 2013, pp. 520–527.
- ¹⁵Shabshelowitz, A. and Gallimore, A. D., "Performance and probe measurements of a radio-frequency plasma thruster," J. Propul. Power, 2013, pp. 1–11.
- ¹⁶Fruchtman, A., Takahashi, K., Charles, C., and Boswell, R., "A magnetic nozzle calculation of the force on a plasma," Phys. Plasmas, Vol. 19, No. 3, 2012, pp. 033507.
- ¹⁷Cox, W., Charles, C., Boswell, R. W., and Hawkins, R., "Spatial retarding field energy analyzer measurements downstream of a helicon double layer plasma," Appl. Phys. Lett., Vol. 93, No. 7, 2008, pp. 071505.
- ¹⁸Deline, C. A., Bengtson, R. D., Breizman, B. N., Tushentsov, M. R., Jones, J. E., Chavers, D. G., Dobson, C. C., and Schuettelpelz, B. M., "Plume detachment from a magnetic nozzle," Phys. Plasmas, Vol. 16, 2009, pp. 033502.
- ¹⁹Terasaka, K., Yoshimura, S., Ogiwara, K., Aramaki, M., and Tanaka, M. Y., "Experimental studies on ion acceleration and stream line detachment in a diverging magnetic field," Phys. Plasmas, Vol. 17, No. 7, 2010, pp. 072106.
- ²⁰Olsen, C., Ballenger, M., Carter, M., Diaz, F., Giambusso, M., Glover, T., Ilin, A., Squire, J., Longmier, B., Bering III, E., and Cloutier, P., "Investigation of Plasma Detachment From a Magnetic Nozzle in the Plume of the VX-200 Magnetoplasma Thruster," 2014.
- ²¹Little, J. and Choueiri, E., "Critical Condition for Plasma Confinement in the Source of a Magnetic Nozzle Flow," 2014.
- ²²Laffeur, T., Charles, C., and Boswell, R., "Ion beam formation in a very low magnetic field expanding helicon discharge," Phys. Plasmas, Vol. 17, 2010, pp. 043505.
- ²³Sudit, I. D. and Chen, F. F., "RF compensated probes for high-density discharges," Plasma Sources Sci. Technol., Vol. 3, No. 2, 1994, pp. 162.
- ²⁴Sheehan, J. P. and Hershkowitz, N., "Emissive probes," Plasma Sources Science and Technology, Vol. 20, No. 6, 2011, pp. 063001.
- ²⁵Iizuka, S., Michelsen, P., Rasmussen, J. J., Schrittwieser, R., Hatakeyama, R., Saeki, K., and Sato, N., "A method for measuring fast time evolutions of the plasma potential by means of a simple emissive probe," Journal of Physics E: Scientific Instruments, Vol. 14, No. 11, 1981, pp. 1291.
- ²⁶Dorf, L., Raitses, Y., and Fisch, N. J., "Electrostatic probe apparatus for measurements in the near-anode region of Hall thrusters," Review of scientific instruments, Vol. 75, No. 5, 2004, pp. 1255–1260.
- ²⁷Brown, D. L. and Gallimore, A. D., "Evaluation of ion collection area in Faraday probes," Review of Scientific Instruments, Vol. 81, No. 6, 2010, pp. 063504.
- ²⁸Sommerville, J. D. and King, L. B., "Hall-Effect Thruster–Cathode Coupling, Part II: Ion Beam and Near-Field Plume," Journal of Propulsion and Power, Vol. 27, No. 4, 2011, pp. 754–767.
- ²⁹Ahedo, E. and Merino, M., "Two-dimensional plasma expansion in a magnetic nozzle: Separation due to electron inertia," Phys. Plasmas, Vol. 19, No. 8, 2012, pp. 083501.
- ³⁰Pottinger, S., Lappas, V., Charles, C., and Boswell, R. W., "Performance characterization of a helicon double layer thruster using direct thrust measurements," J. Phys. D: Appl. Physics, Vol. 44, No. 23, 2011, pp. 235201.
- ³¹Andersen, S., Jensen, V. O., Nielsen, P., and D'Angelo, N., "Continuous supersonic plasma wind tunnel," Phys. Fluids, Vol. 12, 1969, pp. 557.
- ³²Landau, L. and Lifshitz, E., Statistical physics, part I, 1980.
- ³³Little, J. M. and Choueiri, E. Y., "The influence of induced currents on magnetic nozzle acceleration and plasma detachment," Proceedings of 46th Joint Propulsion Conference, Nashville, TN, No. AIAA 2010-6615, 2010.
- ³⁴Little, J. M., Rubin, A. S., and Choueiri, E. Y., "Similarity Parameter Evolution within a Magnetic Nozzle with Applications to Laboratory Plasmas," .
- ³⁵Merino, M. and Ahedo, E., "Influence of electron and ion thermodynamics on the magnetic nozzle plasma expansion," .
- ³⁶Longmier, B., Bering, E., Carter, M., and *et al.*, "Ambipolar ion acceleration in an expanding magnetic nozzle," Plasma Sources Sci. Technol., Vol. 20, 2011, pp. 015007.
- ³⁷Sheehan, J., Longmier, B., Bering, E., Olsen, C., Squire, J., Ballenger, M., Carter, M., Cassady, L., Díaz, F. C., Glover, T., et al., "Temperature gradients due to adiabatic plasma expansion in a magnetic nozzle," Plasma Sources Sci. and Tech., Vol. 23, No. 4, 2014, pp. 045014.
- ³⁸Charles, C., Boswell, R., and Takahashi, K., "Boltzmann expansion in a radiofrequency conical helicon thruster operating in xenon and argon," Applied Physics Letters, Vol. 102, No. 22, 2013, pp. 223510.
- ³⁹Rao, S. and Singh, N., "Numerical simulation of current-free double layers created in a helicon plasma device," Physics of Plasmas (1994-present), Vol. 19, No. 9, 2012, pp. 093507.
- ⁴⁰Saha, S., Raychaudhuri, S., Chowdhury, S., Janaki, M., and Hui, A., "Two-dimensional double layer in plasma in a diverging magnetic field," Phys. Plasmas, Vol. 19, No. 9, 2012, pp. 092502.